Editors' Suggestion

Out-of-plane corrugations in graphene based van der Waals heterostructures

Simon Zihlmann [1,*,†] Péter Makk,[1,2,*,‡] Mirko K. Rehmann,[1,3] Lujun Wang [1,3] Máté Kedves,[2] David I. Indolese [1]
Kenji Watanabe,[4] Takashi Taniguchi,[5] Dominik M. Zumbühl,[1,3] and Christian Schönenberger [1,3]

[1]*Department of Physics, University of Basel, Klingelbergstrasse 82, CH-4056 Basel, Switzerland*
[2]*Department of Physics, Budapest University of Technology and Economics and Nanoelectronics 'Momentum' Research
Group of the Hungarian Academy of Sciences, Budafoki ut 8, 1111 Budapest, Hungary*
[3]*Swiss Nanoscience Institute, University of Basel, Klingelbergstrasse 82, CH-4056 Basel, Switzerland*
[4]*Research Center for Functional Materials, National Institute for Materials Science, 1-1 Namiki, Tsukuba 305-0044, Japan*
[5]*International Center for Materials Nanoarchitectonics, National Institute for Material Science, 1-1 Namiki, Tsukuba 305-0044, Japan*

Two-dimensional (2D) materials are usually envisioned as flat, truly 2D layers. However out-of-plane corrugations are inevitably present in these materials. In this paper, we show that graphene flakes encapsulated between insulating crystals (hexagonal boron nitride, WSe_2), although having large mobilities, surprisingly contain out-of-plane corrugations. The height fluctuations of these corrugations are revealed using weak-localization measurements in the presence of a static in-plane magnetic field. Due to the random out-of-plane corrugations, the in-plane magnetic field results in a random out-of-plane component to the local graphene plane, which leads to a substantial decrease of the phase coherence time. Atomic force microscope measurements also confirm a long-range height modulation present in these crystals. Our results suggest that phase coherent transport experiments relying on purely in-plane magnetic fields in van der Waals heterostructures have to be taken with serious care.

I. INTRODUCTION

From thermodynamical considerations it was long thought that two-dimensional (2D) crystals cannot exist at nonzero temperatures [1–4]. Therefore, it came as a big surprise when graphene (Gr) [5], a truly single layer of graphite, was first discovered. In the following years several other crystals followed [6], among which the transition metal dichalcogenides (TMDCs) are maybe the most famous. The existence of these crystals was attributed to either the presence of the substrate or the appearance of out-of-plane corrugations in the layer [7,8]. Both arguments effectively lift the two-dimensionality of the crystals.

Out-of-plane corrugations and ripples have been observed in graphene by both atomic force microscopy (AFM) and transmission electron microscopy (TEM) studies [7,9,10]. These can originate for thermodynamic reasons, from straining during exfoliation, or from the underlying substrate corrugations. It was found that graphene placed on SiO_2 conformally deforms, resulting in out-of-plane corrugations [11,12]. This has a strong impact on the transport properties. On the one hand, it can reduce the mobility by introducing strain-induced scalar and vector potentials which lead to long-range disorder and hence to additional scattering [13–16]. On the other hand, a more direct and striking consequence can

be observed if the system is placed into an in-plane magnetic field. Random out-of-plane magnetic field components originate from the corrugated graphene sheet, as shown in Fig. 1(a). The corrugations are described by their rms height Z and correlation length R. The resulting random out-of-plane magnetic fields can be seen as random vector potentials that lead to substantial dephasing in weak-localization measurements, as demonstrated by Lundeberg and Folk [17].

With the introduction of hexagonal boron nitride (hBN) as a substrate for graphene devices [18,19], not only a more silent dielectric but also an atomically smooth substrate was found. Recently, TMDCs have emerged as an alternative substrate for exceptionally clean graphene devices [20–24]. However, the remaining mobility-limiting disorder has not yet been identified in these van der Waals (vdW) heterostructures. Strong evidence for strain fluctuations as the remaining disorder has been found in single-layer graphene [14,15] as well as in bilayer graphene devices [25]. Furthermore, in our recent study we could *in situ* tune and increase the mobility of hBN-encapsulated graphene devices by applying a global uniaxial strain to our heterostructures [16]. In doing so, random strain fluctuations are reduced, and hence, the mobility is increased. In principle, strain fluctuations can be of either in-plane or out-of-plane nature. However, the fact that they are tunable with global uniaxial strain [16] and the fact that they are reduced by AFM ironing [15] hints at out-of-plane corrugations as the dominant source of nanometer strain fluctuations.

In this work we present phase coherent magnetotransport studies on several devices encapsulated in hBN or between WSe_2 and hBN. The measured phase coherence time gives

---

*These authors contributed to this work.
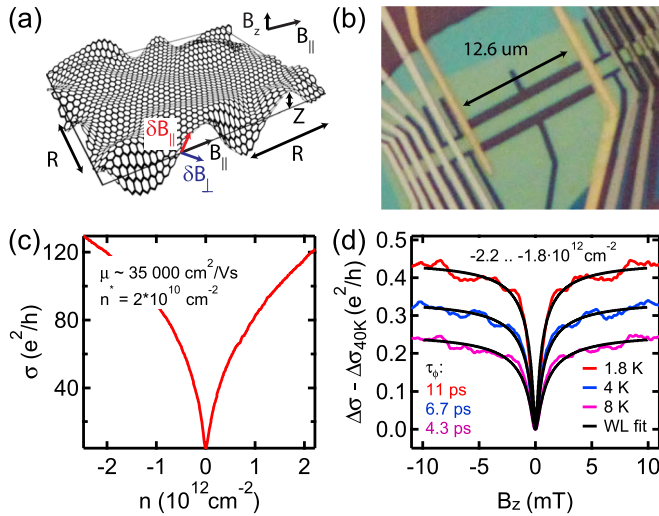†s.zihlmann@unibas.ch
‡peter.makk@mail.bme.hu

FIG. 1. (a) Out-of-plane corrugations in a graphene lattice (exaggerated) with lateral correlation length R and rms height Z. A uniform in-plane magnetic field $B_\parallel$ (black) will lead to a random surface normal ($\delta B_\perp$, blue) and a parallel ($\delta B_\parallel$, red) component. A homogeneous out-of-plane magnetic field B_z is used to study phase coherent transport. (b) Optical image of device 1 (hBN/Gr/hBN). (c) Two-terminal conductivity of device 1 as a function of charge carrier density. (d) Ensemble-averaged weak-localization correction at different temperatures at a hole doping of $-2.2 \times 10^{12} < n < -1.8 \times 10^{12}$ cm^{-2} and zero in-plane magnetic field.

valuable insight into out-of-plane corrugations. By applying an in-plane magnetic field the phase coherence time drops even for devices appearing at first sight to be flat and bubble free. The measurements are well accounted for by the model introduced in Refs. [17,26] and are also in accordance with detailed AFM studies. Our measurements are unambiguous proof of the presence of out-of-plane corrugations in vdW heterostructures. These corrugations could be the origin of the random strain fluctuations limiting the charge carrier mobility and could limit phase coherent transport experiments in the presence of an in-plane magnetic field.

II. RESULTS

In the following, experimental data for three different vdW heterostructures are presented. An overview of the three samples is given in Table I in Appendix A.

An optical image of device 1 after fabrication is shown in Fig. 1(b). It is a two-terminal hBN/Gr/hBN heterostructure with a large aspect ratio (length/width), which makes it ideal for magnetoconductance measurements. The conductivity as a function of charge carrier density is shown in Fig. 1(c), from which we extract a mobility of 35 000 cm^2 V^{-1} s^{-1} and a residual doping of 2×10^{10} cm^{-2}. At low temperature, phase coherent transport leads to weak localization, as shown in Fig. 1(d). Here, we plot an ensemble-averaged quantum correction to the magnetoconductivity at different temperatures, which we obtain by subtracting the classical magnetoconductivity measured at 40 K from the low-temperature measurements. The quantum correction to the magnetoconductivity can be fitted by the standard weak localization (WL)

formula for graphene [27]:

$$\Delta\sigma(B) = \frac{e^2}{\pi h}\left[F\left(\frac{\tau_B^{-1}}{\tau_\phi^{-1}}\right) - F\left(\frac{\tau_B^{-1}}{\tau_\phi^{-1} + 2\tau_{iv}^{-1}}\right) - 2F\left(\frac{\tau_B^{-1}}{\tau_\phi^{-1} + \tau_{iv}^{-1} + \tau_*^{-1}}\right)\right],\tag{1}$$

where $F(x) = \ln(x) + \Psi(1/2 + 1/x)$, with $\Psi(x)$ being the digamma function; $\tau_B^{-1} = 4DeB/\hbar$, where D is the diffusion constant; τ_ϕ is the phase coherence time; τ_{iv} is the intervalley scattering time; and τ_* is the intravalley scattering time. We fit the curves corresponding to the three different temperatures within the same fitting procedure (global fit), where only τ_ϕ is allowed to change with temperature to extract all relevant scattering timescales [28]. We generally find phase coherence times on the order of a few picoseconds at a temperature of a few kelvins and an intervalley scattering time τ_{iv} of 6.9×10^{-12} s and very small intravalley scattering times $\tau_* \lesssim 1 \times 10^{-13}$ s. As long as τ_ϕ is much longer than τ_{iv} and τ_*, graphene exhibits WL behavior [29], and the curvature of the magnetoconductivity at zero out-of-plane magnetic field is a good measure of τ_ϕ.

In order to probe the out-of-plane corrugations we study phase coherent transport as a function of small out-of-plane magnetic fields in the presence of large, static in-plane magnetic fields. It is obvious that a homogeneous in-plane magnetic field leads to random out-of-plane components $\delta B_\perp$ if the graphene sheet has out-of-plane corrugations [see Fig. 1(a)]. These random out-of-plane magnetic field components can be described as random vector potentials that affect phase coherent transport.

The first experiments were realized on Si inversion layers [30,31] and two-dimensional electron gases in GaAs heterojunctions [30]. A direct correlation between the topographic morphology and the dephasing rate has been found. Motivated by these findings, Mathur and Baranger calculated the additional dephasing for a two-dimensional electron gas originating from Gaussian correlated corrugations in the presence of an in-plane magnetic field [26]:

$$\tau_\phi^{-1} \to \tau_\phi^{-1} + \sqrt{\pi}\frac{e^2}{\hbar^2}vZ^2RB_\parallel^2.\tag{2}$$

Here, Z is the rms of the corrugation height, R is the lateral correlation length of the corrugations, $B_\parallel$ is the in-plane magnetic field, v is the Fermi velocity, and constants e and $\hbar$ are the electronic charge and the reduced Planck's constant, respectively.

The quantum correction to the magnetoconductivity for different in-plane magnetic fields is shown in Fig. 2(a). Here, we show a representative data set for hole doping. Single WL curves represent an ensemble-averaged measurement over a density range of -2.2×10^{12} to -1.8×10^{12} cm^{-2}. Similar effects have been observed for electron doping. Different colors represent WL curves measured at different in-plane magnetic fields. As the in-plane field increases, the dip around zero magnetic field gets less pronounced, and the overall magnetoconductance decreases. These changes can be understood by a reduced phase coherence time τ_ϕ.
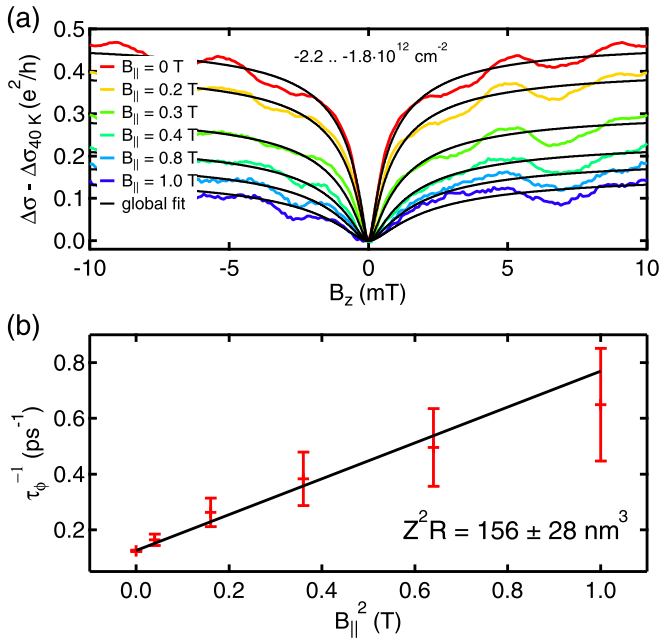
FIG. 2. (a) WL of device 1 for different values of in-plane field $B_\parallel$ at a temperature of 1.8 K. The fitted dephasing rate τ_ϕ^{-1} as a function of $B_\parallel^2$ is shown in (b).

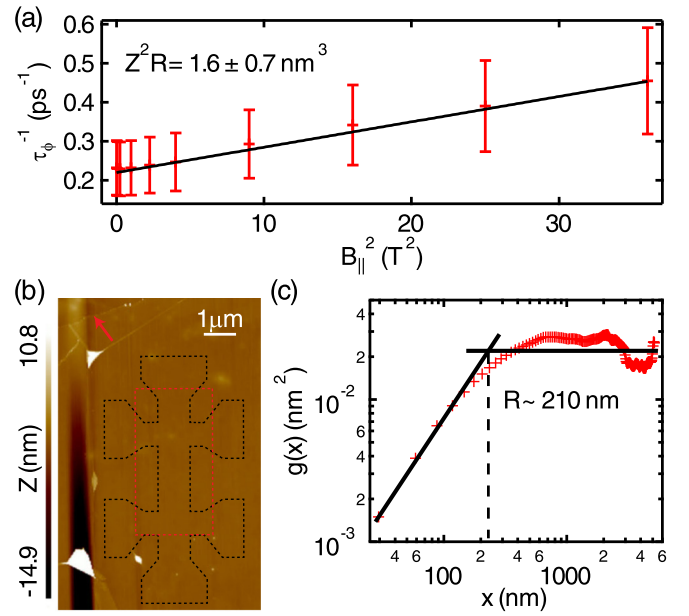

FIG. 3. (a) Fitted dephasing rate of device 2 as a function of $B_\parallel^2$. A ripple volume of $1.6\,\mathrm{nm}^3$ is extracted. (b) AFM image of the graphene flake on top of the bottom hBN crystal. The graphene flake outline is marked by the red arrow. The location of the Hall bar is indicated by the black dashed line, and the area used for the AFM analysis is highlighted by a red dashed rectangle. (c) Height-height correlation of device 2 extracted from the AFM measurement in (b). A correlation length of 210 nm and an average height fluctuation of $94.4 \pm 1.2\,\mathrm{pm}$ are found.

In order to perform a quantitative analysis, we apply a global fit (fitting all the curves with different $B_\parallel$ at the same time) where only τ_ϕ is allowed to vary since neither τ_{iv} nor τ_* is expected to be affected by $B_\parallel$. The extracted dephasing rate τ_ϕ^{-1} is shown in Fig. 2(b) as a function of $B_\parallel^2$. Clear linear behavior is observed that allows us to extract an apparent corrugation volume $Z^2 R = 156 \pm (28)\,\mathrm{nm}^3$ using Eq. (2). The relatively large apparent corrugation volume, which is much larger than the previously reported value of $1.7\,\mathrm{nm}^3$ for graphene on SiO_2 [17], can be explained by the presence of bubbles in the device. Bubbles with contaminations are known to spontaneously form at interfaces of vdW heterostructures [20,32] and were confirmed by optical and AFM images of device 1. Therefore, it is not surprising that additional dephasing is observed when device 1 is placed in an in-plane magnetic field. Strictly speaking, Eq. (2) holds only for random corrugations, which is not fulfilled for device 1, which contains bubbles at the graphene/hBN interfaces. It is therefore not straightforward to link the apparent corrugation volume extracted by transport to the true geometrical corrugation of the graphene layer.

However, we also found an additional dephasing in much cleaner and essentially bubble-free hBN/Gr/hBN heterostructures. We have measured the phase coherence time as a function of in-plane magnetic field $B_\parallel$ for device 2 as well. Here, we directly show in Fig. 3(a) the extracted dephasing rate as a function of $B_\parallel^2$ of device 2 at a doping of 0.3×10^{12} to $1.2 \times 10^{12}\,\mathrm{cm}^{-2}$. The dephasing rate was extracted from the curvature of the magnetoconductivity at zero out-of-plane magnetic field (see Fig. 8 in Appendix B for more details). This device, which is free from bubbles [confirmed by AFM measurements; see Fig. 3(b)], shows a corrugation volume $Z^2 R = 1.6 \pm (7)\,\mathrm{nm}^3$. This is two orders

of magnitude smaller than the extracted volume for device 1, which contains bubbles, and surprisingly close to the corrugation volume of graphene on SiO_2. It is important to note that the random corrugation of this device [see the AFM image in Fig. 3(b)] allows a direct comparison of the corrugation volume extracted by transport measurements with the true geometrical corrugations.

The additional dephasing in an in-plane magnetic field gives access only to the total corrugation volume $Z^2 R$ and not to the individual contributions of height Z and radius R. We used high-resolution AFM images to extract the standard deviation of a Gaussian height distribution that corresponds to the corrugation height Z and the height-height correlation length that corresponds to the corrugation radius R. An AFM image of device 2, with the outline of the Hall bar before placing the top hBN, is shown in Fig. 3(b) (see Appendix A for further fabrication details). From the height distribution, we extracted $Z = 94.4 \pm 1.2\,\mathrm{pm}$ (see Fig. 9 in Appendix C). In addition, the same data set is used to extract the height-height correlation length, which is the characteristic length scale for the corrugations. As shown in Fig. 3(c), the correlation length R corresponds to the crossover between the small and large length scale behaviors of the correlation function, as evident in a log-log plot. We find $R \sim 210\,\mathrm{nm}$ for this device. Analysis of further graphene/hBN half stacks prepared in the same manner revealed very similar values for the height distribution and lateral correlation length. Thus, we find a corrugation volume by analyzing AFM images
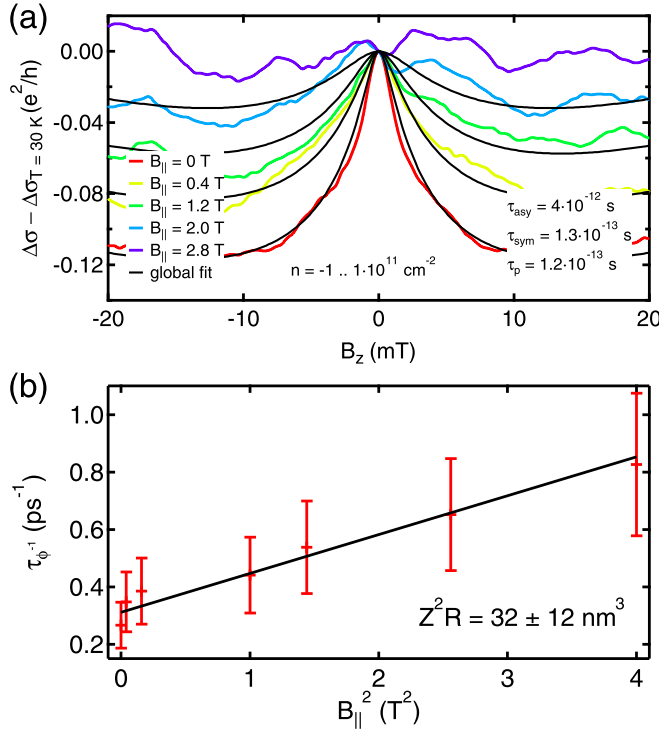
FIG. 4. (a) WAL of device 3 for different values of in-plane magnetic field $B_\parallel$ at a temperature of 1.8 K. (b) The fitted dephasing rate τ_ϕ^{-1} as a function of $B_\parallel^2$.

$Z^2 R_{\text{AFM}} \sim 1.9 \, \text{nm}^3$. This independent rough estimation of the corrugation volume matches the corrugation volume extracted from transport measurements well.

Even though graphene is sandwiched between two layers of atomically flat hBN crystals, out-of-plane corrugations are present. The corrugation volume in bubble-free hBN encapsulated graphene ($1.6 \, \text{nm}^3$) is similar to the corrugation volume of SiO_2-supported graphene ($1.7 \, \text{nm}^3$). However, in the case of hBN-encapsulated graphene, the corrugations have a smaller height but larger lateral extension compared to the relatively short length scales in graphene on SiO_2, which is on the order of a few nanometers [9,17].

Out-of-plane corrugations are not limited to hBN-encapsulated graphene but are a generic phenomenon in vdW heterostructures. Here, we present phase coherent transport in hBN/Gr/WSe$_2$ heterostructures, where additional dephasing is observed when an in-plane magnetic field is applied. Figure 4(a) shows the quantum correction of the magnetoconductivity that exhibits weak antilocalization (WAL) due to graphene's proximity to the TMDC WSe$_2$ [23]. In the case of graphene, the quantum correction to the magnetoconductivity $\Delta\sigma$ in the presence of strong spin-orbit coupling is given by [33]

$$\Delta\sigma(B) = -\frac{e^2}{2\pi h}\left[F\left(\frac{\tau_B^{-1}}{\tau_\phi^{-1}}\right) - F\left(\frac{\tau_B^{-1}}{\tau_\phi^{-1} + 2\tau_{asy}^{-1}}\right) \right. $$
$$\left. - 2F\left(\frac{\tau_B^{-1}}{\tau_\phi^{-1} + \tau_{asy}^{-1} + \tau_{sym}^{-1}}\right) \right], \quad (3)$$

where $F(x) = \ln(x) + \Psi(1/2 + 1/x)$, with $\Psi(x)$ being the digamma function; $\tau_B^{-1} = 4DeB/\hbar$, where D is the diffusion constant; τ_ϕ is the phase coherence time; and τ_{asy} (τ_{sym}) is the spin-orbit scattering time that takes into account only spin-orbit terms that are asymmetric (symmetric) in the $z \to -z$ direction. Assuming that τ_{asy} and τ_{sym} are independent of $B_\parallel$, we perform a global fit where only τ_ϕ is allowed to vary with $B_\parallel$. We have also varied the spin-orbit times, which essentially did not change within the limits of the extraction method (see also Ref. [23] for further information). The extracted dephasing rate scales linearly as a function of $B_\parallel^2$, as shown in Fig. 4(b). Using Eq. (2), a corrugation volume $Z^2 R = 32 \pm (12) \text{nm}^3$ is extracted. This is roughly an order of magnitude smaller (larger) than in device 1 (2).

It is known that an additional dephasing due to spin orbit might occur if an in-plane magnetic field is applied [33]. This would result in a crossover from WAL to WL behavior with increasing $B_\parallel$. This effect could, in principle, qualitatively explain the increased dephasing in device 3 at first sight. However, at sufficiently large $B_\parallel$, WL behavior should be recovered in this case. We did not observe any WL behavior in the range of 3 to 9 T in in-plane field [23]. The absence of a WL dip at large $B_\parallel$ and the fact that the dephasing rate scales linearly with $B_\parallel^2$ point to the fact that out-of-plane corrugations are most likely the main source of dephasing in the presence of an in-plane magnetic field.

III. DISCUSSION

Despite the fact that hBN crystals are atomically flat and of high quality, graphene encapsulated between two such crystals exhibits out-of-plane corrugations. The corrugation volume extracted from phase coherent transport measurements varies among different vdW heterostructures depending on their interface and crystal quality. The large apparent corrugation volume observed in device 1 obviously originates from bubbles at the Gr/hBN interface and can be avoided by utilizing heterostructures with a better interface quality or by designing the active area of the device in a bubble-free part of the heterostructure. However, in essentially bubble-free heterostructures, out-of-plane corrugations are still present. Whereas for device 3 the vdW interface might still be the limiting factor in terms of the origin of out-of-plane corrugations, this is certainly not the case in device 2, where AFM images show a smooth, atomically flat surface without any bubbles or contaminations. Here, a different explanation for the presence of out-of-plane corrugations has to be invoked. One possibility is that the crystal quality of hBN might influence the remaining out-of-plane corrugations since defects in the hBN crystal (also in layers far away from the interface with the graphene) might lead to long-range height fluctuations [34]. Moreover, residues trapped at the bottom hBN-SiO_2 interface might lead to long-range height fluctuations at the top of the bottom hBN as well.

Our results are in agreement with previous measurements on graphene on SiO_2 substrate [17]. It is clear that devices with bubbles exhibit a larger corrugation volume than devices on a clean SiO_2 surface. However, it is surprising that not even the best hBN/Gr/hBN devices show a smaller corrugation volume than devices on SiO_2 substrates. It is important to note

that even though the corrugation volume is similar, the lateral correlation length is much longer, and the height variation is considerably smaller for vdW heterostructures ($Z \sim 0.1$ nm, $R \sim 200$ nm) compared to a SiO_2 substrate ($Z \sim 0.4$ nm, $R \sim 5$ nm [11,12]). Therefore, the deformations of the graphene lattice and hence the random strain fluctuations are greatly reduced in graphene in vdW heterostructures compared to graphene on SiO_2 substrates. This might be one of the reasons why the graphene quality in fully encapsulated graphene can be exceptionally good.

Finally, we would like to raise the point that the presence of out-of-plane corrugations (even in the cleanest devices) might impose severe limitations on phase coherent experiments relying on large in-plane magnetic fields. This, for example, prevents one from studying the transition from WAL to WL in graphene with spin-orbit coupling triggered by an in-plane magnetic field [23,33]. In addition, the magnitude of the supercurrent in a graphene based Josephson junction in an in-plane magnetic field could be reduced due to a reduced phase coherence time.

IV. CONCLUSION

In conclusion, phase coherent transport has shown that out-of-plane corrugations are present in vdW heterostructures. The corrugation volume strongly depends on the interface quality between graphene and other 2D materials (e.g., hBN and WSe_2) but is nonzero even for the best interface and device quality ($\mu \sim 100\,000$ cm^2 V^{-1} s^{-1}). The presence of out-of-plane corrugations implies distortions of the graphene lattice and hence the presence of random strain fluctuations. While the corrugation volume for the cleanest hBN/Gr/hBN device is similar to graphene on SiO_2, its effect on transport is greatly reduced because of the long-range nature of the corrugations in hBN/Gr/hBN (smaller strain fluctuations). Nonetheless, phase coherent experiments relying on large in-plane magnetic fields could suffer from the out-of-plane corrugations due to a reduced phase coherence time.

APPENDIX A: OVERVIEW OF THE MEASURED DEVICES

Table I shows an overview of the three devices.

1. Fabrication of device 1 and device 3

The vdW heterostructures of device 1 and device 3 were assembled using a dry pickup method [35] and Cr/Au one-dimensional edge contacts were used [19]. After shaping the vdW heterostructure into a Hall-bar geometry by a reactive ion etching plasma employing SF_6 as the main reactive gas, Ti/Au top gates with an MgO dielectric layer were fabricated on device 3. A heavily doped silicon substrate with 300 nm SiO_2 was used as a global back gate for both devices.

AFM and optical images of device 1 (device 3) are shown in Fig. 5 (Fig. 6).

2. Fabrication of device 2

Device 2 was not fabricated using the dry pickup method but relying on a wet process in which the graphene is transferred by a poly(methyl methacrylate) (PMMA) membrane on a hBN flake [18]. After PMMA removal in acetone, the sample was annealed at 450 °C in a hydrogen atmosphere (1.7 mbar). Clean and wrinkle-free areas were identified by imaging the heterostructure by noncontact AFM prior to the

TABLE I. Overview of the three devices. D, l_{mfp}, τ_ϕ, l_ϕ, and B_{tr} are given for the density range that was used for the evaluation of the out-of-plane corrugations in the density interval n_{eval}. Phase coherence time and length are measured at a fridge temperature of 1.8 K for devices 1 and 3 and 30 mK for device 2. Na stand for not available.

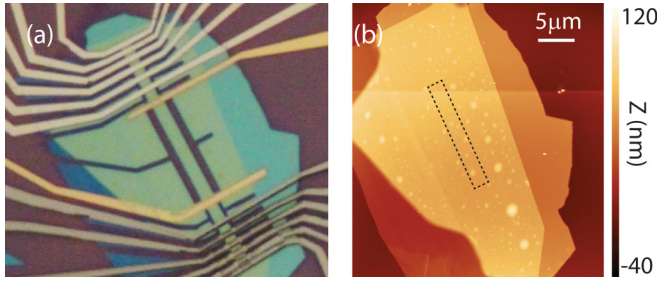|	μ (cm^2 V^{-1} s^{-1})	n_{eval} (10^{12}cm^{-2})	D (m^2/s)	l_{mfp} (nm)	τ_ϕ (ps)	l_ϕ (μm)	B_{tr} (mT)	$Z^2 R_{tr}$ (nm^3)	$Z^2 R_{AFM}$ (nm^3)
Device 1 hBN/Gr/hBN	35 000	-2.2 to -1.8	0.32	640	8	1.6	10	125	na
Device 2 hBN/Gr/hBN	120 000	0.3 to 1.2	0.23	460	4.3	0.98	20	1.6	1.9
Device 3 WSe$_2$/Gr/hBN	130 000	-0.1 to 0.1	0.075	150	3.8	0.53	180	31	na

FIG. 5. (a) Optical image and (b) AFM image of the full vdW heterostructure of device 1 with the device outline overlaid.

deposition of a top hBN layer to protect the graphene from further fabrication steps. These AFM images were also used to extract the data shown in Fig. 3. The deposition of the top hBN could, in principle, induce additional corrugation. The device shaping as well as the contact deposition was performed in the same way as for device 1 and device 3.

3. Measurements and data analysis

Standard low-frequency lock-in techniques were used to measure two- and four-terminal conductances and resistances. Weak (anti)localization was measured at a temperature of 1.8 K, whereas a classical background was measured at sufficiently large temperatures of 30 to 50 K for device 1 and device 3. Device 2 was measured at 30 mK, and no classical background was subtracted. A vector magnet was used to independently control the in-plane ($B_\parallel$) and out-of-plane (B_z) magnetic field components.

The quantum correction to the magnetoconductivity was analyzed only in the interval $|B_z| \leqslant B_{tr}$, where $B_{trans} = \Phi_0/l_{mfp}$ is the so-called transport field that describes the limit of diffusive transport.

The diffusion constant was calculated in the following way:

$$D(n) = \frac{\hbar v_F \sqrt{\pi}}{2e^2} \frac{\sigma(n)}{\sqrt{\sqrt{n^2 + n_*^2}}}, \qquad (A1)$$

where $\hbar$ is the reduced Planck constant, $v_F = 1 \times 10^6$ m/s is the Fermi velocity of graphene, and e is the fundamental unit of charge. The conductivity σ was measured, and n was calculated from a parallel plate capacitor model. The residual
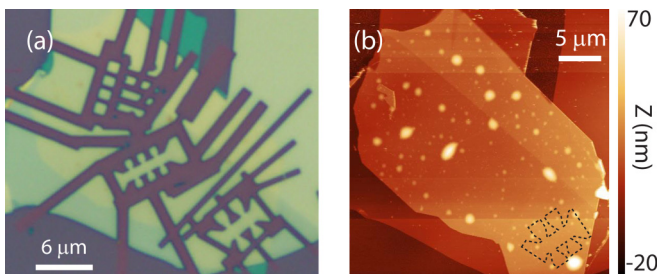

FIG. 6. (a) Optical image and (b) AFM image of the full vdW heterostructure of device 3 that show that the device area is essentially bubble free. Data presented in the main text were taken from the Hall bar outlined in (b).
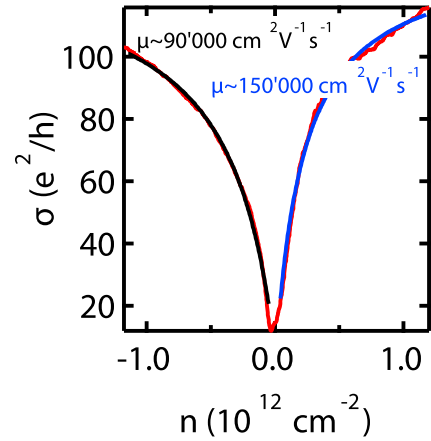

FIG. 7. Two-terminal conductivity as a function of charge carrier density of device 2. A two-parameter model is fit to extract charge carrier mobility and series resistance ($\sim$190 Ω).

doping n^* was used as a cutoff to calculate D around the charge neutrality point.

The main source of uncertainty of the extracted dephasing times originates from the uncertainty in the aspect ratio of the devices (around 30%). Other sources are estimated to have a smaller contribution, which includes the error of the fit to Eqs. (1), (3), and (B1). For device 1, a detailed analysis, including the influence of the uncertainty in the aspect ratio on the fit to Eq. (1), was performed. The maximum relative uncertainty was found to be around 30% (identical to the one from the aspect ratio). Therefore, we used directly a relative uncertainty of 30% for devices 2 and 3.

APPENDIX B: MAGNETOCONDUCTIVITY OF DEVICE 2

Figure 7 shows the gate dependence of the two-terminal conductance of device 2.

Instead of fitting the full WL formula [see eq. (1) for the magnetoconductivity], the phase coherence time τ_ϕ can also be extracted from the curvature of the magnetoconductance σ at zero out-of-plane magnetic field $B_\perp$ [36]:

$$\left.\frac{\partial^2\sigma}{\partial B_\perp^2}\right|_{B_\perp=0} = \frac{16\pi}{3}\frac{e^2}{h}\left(\frac{D\tau_\phi}{h/e}\right)^2, \qquad (B1)$$

where D is the diffusion constant, τ_ϕ is the phase coherence time, and the constants e and h are the electron's charge and Planck's constant, respectively. This is especially useful for very high mobility devices where B_{tr} is very small. Figure 8 shows the magnetoconductivity for electron doping for various in-plane magnetic fields. It is clearly observable that the curvature at zero B_z gets smaller for larger in-plane magnetic field; hence, the phase coherence time is smaller as well.

As stated in the main text, the curvature of the magnetoconductivity around zero magnetic field is a good measure of the phase coherence time if $\tau_\phi \gg \tau_{iv}, \tau_*$ [29]. In this case Eq. (B1) can be applied. We would like to note that the condition $\tau_\phi \gg \tau_*$ is generally fulfilled for hBN-encapsulated graphene (see device 1 and Ref. [14]). Furthermore, a ratio of τ_ϕ/τ_{iv} of 1/2, which might be the case for large in-plane magnetic
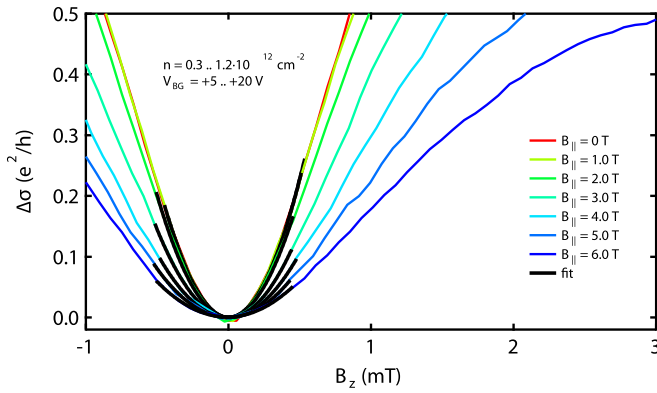
FIG. 8. Magnetoconductivity for various in-plane magnetic fields for electron doping of device 2. The black curves are fits with a parabola to extract the phase coherence time using Eq. (B1).
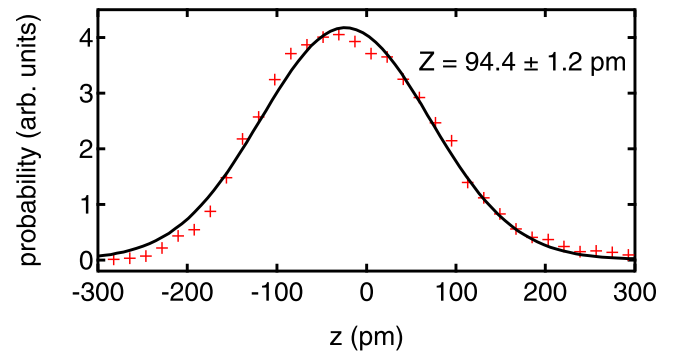

FIG. 9. The height distribution (red crosses) evaluated in the area marked by the red dashed rectangle in Fig. 3(b). A Gaussian fit (black solid line) yields $Z = 94.4 \pm 1.2$ pm.

fields, leads to an uncertainty of only ∼25% in the extraction of τ_ϕ with Eq. (B1).

APPENDIX C: ADDITIONAL INFORMATION ON THE AFM ANALYSIS

The AFM analysis presented in the main text and below was performed on device 2 before placing the top hBN. The area marked by the red dashed rectangle in Fig. 3(b), which corresponds to the area where the Hall bar was defined, was used to extract Z and R. Therefore, the AFM analysis and the transport measurements probe the same area. A tilted plane was subtracted from the height data prior to the detailed analysis described in the following.

The rms height Z of the corrugations can directly be extracted from AFM measurements by either calculating it from the raw data (point by point) or fitting the height distribution with a Gaussian model. The point-by-point calculation of Z is given as

$$Z = \sqrt{\frac{1}{N}\sum_{n=1}^{N}(z_n - \bar{z})^2}, \tag{C1}$$

where z_n is the height value of point n and $\bar{z}$ is the average height value of all N points of the AFM image. Additionally, the height distribution, as shown in Fig. 9, can be used to extract Z. We find $Z = 94.4 \pm 1.2$ pm from the width of the height distribution, which is in good agreement with literature values for graphene on hBN [18].

The height-height correlation function in one dimension $g(x) = \langle [z(x_0 + x) - z(x_0)]^2 \rangle$ [9] is defined as follows for a discrete data set:

$$g(x) = \frac{1}{N(M-m)}\sum_{l=1}^{N}\sum_{n=1}^{M-m}(z_{n+m,l} - z_{n,l})^2, \tag{C2}$$

where $m = x/\Delta x$ and Δx is the spacing between two points. Equation (C2) represents the one-dimensional height-height correlation function averaged over N lines of the second lateral dimension, as commonly used in the analysis of AFM images, where $g(x)$ is calculated for the fast scanning directions and averaged over the slow scanning direction. Equation

(C2) was used to calculate $g(x)$, which is shown in Fig. 3(c) in the main text. The correlation length R is identified as the crossover from the polynomial short-range behavior to the constant long-range behavior.

For a Gaussian correlated surface, as assumed by Mathur and Barangar [26] for their calculation, the height-height correlation function takes the form

$$g(x) = 2Z^2\left(1 - e^{-x^2/R^2}\right), \tag{C3}$$

where Z is the rms deviation from the mean height and R is the correlation length. This is a direct result of the assumption of a Gaussian correlated surface that is defined by a height distribution $z(x)$ with zero mean and a variance given by

$$\langle z(x)z(x') \rangle = Z^2 e^{-(x-x')^2/R^2}, \tag{C4}$$

where x and x' are positions along the x direction, Z is the rms height fluctuation, and R is the correlation length.

The crossover between the short-range behavior and the long-range behavior takes place at $R \sim 210$ nm, as indicated by the crossing of the black solid lines in Fig. 3(c) in the main text. In addition, the value for the long-range behavior [$2Z^2$, as given by Eq. (C3) for large, uncorrelated distances] agrees well with Z extracted from the height distribution. Fitting the data with Eq. (C3) results in $Z = 106 \pm 1$ pm and $R = 187 \pm 20$ nm, which give reasonable agreement with the general calculation.

We would like to note that the corrugation volume extracted from transport measurements can directly be compared to the corrugation volume extracted from AFM measurements; see Refs. [26,31,37] for further information. In order for Eq. (2) to be valid, it is assumed that the correlation length R is of short range compared to the mean free path l_{mfp} [26]. This condition is fulfilled for device 2, where the correlation length has been determined by AFM measurements. It is a question whether this condition is valid for devices 1 and 3. However, the experimental finding ($\tau_\phi^{-1} \propto B_\parallel^2$) suggests also a homogeneous broadening described by Eq. (2).

[1] R. Peierls, Bemerkungen über Umwandlungstemperaturen, Helv. Phys. Acta **7**, 81 (1934).

[2] R. Peierls, Quelques propriétés typiques des corps solides, Ann. Inst. Henri Poincare **5**, 177 (1935).

[3] L. D. Landau, Zur Theorie der Phasenumwandlungen II, Phys. Z. Sowjet. **11**, 545 (1937).

[4] N. D. Mermin, Crystalline order in two dimensions, Phys. Rev. **176**, 250 (1968).

[5] K. S. Novoselov, A. K. Geim, S. V. Morozov, D. Jiang, Y. Zhang, S. V. Dubonos, I. V. Grigorieva, and A. A. Firsov, Electric field effect in atomically thin carbon films, Science **306**, 666 (2004).

[6] K. S. Novoselov, D. Jiang, F. Schedin, T. J. Booth, V. V. Khotkevich, S. V. Morozov, and A. K. Geim, Two-dimensional atomic crystals, Proc. Natl. Acad. Sci. USA **102**, 10451 (2005).

[7] J. C. Meyer, A. K. Geim, M. I. Katsnelson, K. S. Novoselov, T. J. Booth, and S. Roth, The structure of suspended graphene sheets, Nature (London) **446**, 60 (2007).

[8] A. Fasolino, J. H. Los, and M. I. Katsnelson, Intrinsic ripples in graphene, Nat. Mater. **6**, 858 (2007).

[9] M. Ishigami, J. H. Chen, W. G. Cullen, M. S. Fuhrer, and E. D. Williams, Atomic structure of graphene on SiO_2, Nano Lett. **7**, 1643 (2007).

[10] C. H. Lui, L. Liu, K. F. Mak, G. W. Flynn, and T. F. Heinz, Ultraflat graphene, Nature (London) **462**, 339 (2009).

[11] V. Geringer, M. Liebmann, T. Echtermeyer, S. Runte, M. Schmidt, R. Rückamp, M. C. Lemme, and M. Morgenstern, Intrinsic and Extrinsic Corrugation of Monolayer Graphene Deposited on SiO_2, Phys. Rev. Lett. **102**, 076102 (2009).

[12] W. G. Cullen, M. Yamamoto, K. M. Burson, J. H. Chen, C. Jang, L. Li, M. S. Fuhrer, and E. D. Williams, High-Fidelity Conformation of Graphene to SiO_2 Topographic Features, Phys. Rev. Lett. **105**, 215504 (2010).

[13] M. I. Katsnelson and A. K. Geim, Electron scattering on microscopic corrugations in graphene, Philos. Trans. R. Soc. A **366**, 195 (2008).

[14] N. J. G. Couto, D. Costanzo, S. Engels, D.-K. Ki, K. Watanabe, T. Taniguchi, C. Stampfer, F. Guinea, and A. F. Morpurgo, Random Strain Fluctuations as Dominant Disorder Source for High-Quality On-Substrate Graphene Devices, Phys. Rev. X **4**, 041019 (2014).

[15] Y. Kim, P. Herlinger, T. Taniguchi, K. Watanabe, and J. H. Smet, Reliable postprocessing improvement of van der Waals heterostructures, ACS Nano **13**, 14182 (2019).

[16] L. Wang, P. Makk, S. Zihlmann, A. Baumgartner, D. I. Indolese, K. Watanabe, T. Taniguchi, and C. Schönenberger, Mobility Enhancement in Graphene by in situ Reduction of Random Strain Fluctuations, Phys. Rev. Lett. **124**, 157701 (2020).

[17] M. B. Lundeberg and J. A. Folk, Rippled Graphene in an In-Plane Magnetic Field: Effects of a Random Vector Potential, Phys. Rev. Lett. **105**, 146804 (2010).

[18] C. R. Dean, A. F. Young, I. Meric, C. Lee, L. Wang, S. Sorgenfrei, K. Watanabe, T. Taniguchi, P. Kim, K. L. Shepard, and J. Hone, Boron nitride substrates for high-quality graphene electronics, Nat. Nanotechnol. **5**, 722 (2010).

[19] L. Wang, I. Meric, P. Y. Huang, Q. Gao, Y. Gao, H. Tran, T. Taniguchi, K. Watanabe, L. M. Campos, D. A. Muller, J. Guo, P. Kim, J. Hone, K. L. Shepard, and C. R. Dean, One-dimensional electrical contact to a two-dimensional material, Science **342**, 614 (2013).

[20] A. V. Kretinin, Y. Cao, J. S. Tu, G. L. Yu, R. Jalil, K. S. Novoselov, S. J. Haigh, A. Gholinia, A. Mishchenko, M. Lozada, T. Georgiou, C. R. Woods, F. Withers, P. Blake, G. Eda, A. Wirsig, C. Hucho, K. Watanabe, T. Taniguchi, A. K. Geim, and R. V. Gorbachev, Electronic properties of graphene encapsulated with different two-dimensional atomic crystals, Nano Lett. **14**, 3270 (2014).

[21] C.-P. Lu, G. Li, K. Watanabe, T. Taniguchi, and E. Y. Andrei, MoS_2: Choice Substrate for Accessing and Tuning the Electronic Properties of Graphene, Phys. Rev. Lett. **113**, 156804 (2014).

[22] L. Banszerus, H. Janssen, M. Otto, A. Epping, T. Taniguchi, K. Watanabe, B. Beschoten, D. Neumaier, and C. Stampfer, Identifying suitable substrates for high-quality graphene-based heterostructures, 2D Mater. **4**, 025030 (2017).

[23] S. Zihlmann, A. W. Cummings, J. H. Garcia, M. Kedves, K. Watanabe, T. Taniguchi, C. Schönenberger, and P. Makk, Large spin relaxation anisotropy and valley-Zeeman spin-orbit coupling in WSe_2/graphene/h-BN heterostructures, Phys. Rev. B **97**, 075434 (2018).

[24] L. Banszerus, T. Sohier, A. Epping, F. Winkler, F. Libisch, F. Haupt, K. Watanabe, T. Taniguchi, K. Müller-Caspary, N. Marzari, F. Mauri, B. Beschoten, and C. Stampfer, Extraordinary high room-temperature carrier mobility in graphene-WSe_2 heterostructures, arXiv:1909.09523

[25] S. Engels, B. Terrés, A. Epping, T. Khodkov, K. Watanabe, T. Taniguchi, B. Beschoten, and C. Stampfer, Limitations to Carrier Mobility and Phase-Coherent Transport in Bilayer Graphene, Phys. Rev. Lett. **113**, 126801 (2014).

[26] H. Mathur and H. U. Baranger, Random berry phase magnetoresistance as a probe of interface roughness in Si MOSFET's, Phys. Rev. B **64**, 235325 (2001).

[27] E. McCann, K. Kechedzhi, V. I. Fal'ko, H. Suzuura, T. Ando, and B. L. Altshuler, Weak-Localization Magnetoresistance and Valley Symmetry in Graphene, Phys. Rev. Lett. **97**, 146805 (2006).

[28] F. V. Tikhonenko, D. W. Horsell, R. V. Gorbachev, and A. K. Savchenko, Weak Localization in Graphene Flakes, Phys. Rev. Lett. **100**, 056802 (2008).

[29] F. V. Tikhonenko, A. A. Kozikov, A. K. Savchenko, and R. V. Gorbachev, Transition between Electron Localization and Antilocalization in Graphene, Phys. Rev. Lett. **103**, 226801 (2009).

[30] P. M. Mensz, R. G. Wheeler, C. T. Foxon, and J. J. Harris, Determination of spatial potential fluctuations in Si and GaAs inversion layers by weak localization, Appl. Phys. Lett. **50**, 603 (1987).

[31] W. R. Anderson, D. R. Lombardi, R. G. Wheeler, and T. Ma, Determination of Si/SiO_2 interface roughness using weak localization, IEEE Electron Device Lett. **14**, 351 (1993).

[32] S. J. Haigh, A. Gholinia, R. Jalil, S. Romani, L. Britnell, D. C. Elias, K. S. Novoselov, L. A. Ponomarenko, A. K. Geim, and R. Gorbachev, Cross-sectional imaging of individual layers and buried interfaces of graphene-based heterostructures and superlattices, Nat. Mater. **11**, 764 (2012).

[33] E. McCann and V. I. Fal'ko, $z \rightarrow -z$ Symmetry of Spin-Orbit Coupling and Weak Localization in Graphene, Phys. Rev. Lett. **108**, 166606 (2012).

[34] A. P. Rooney, A. Kozikov, A. N. Rudenko, E. Prestat, M. J. Hamer, F. Withers, Y. Cao, K. S. Novoselov, M. I. Katsnelson, R. Gorbachev, and S. J. Haigh, Observing imperfection in atomic interfaces for van der Waals heterostructures, Nano Lett. **17**, 5222 (2017).

[35] P. J. Zomer, M. H. D. Guimarães, J. C. Brant, N. Tombros, and B. J. van Wees, Fast pick up technique for high quality heterostructures of bilayer graphene and hexagonal boron nitride, Appl. Phys. Lett. **105**, 013101 (2014).

[36] S. Lara-Avila, S. Kubatkin, O. Kashuba, J. A. Folk, S. Lüscher, R. Yakimova, T. J. B. M. Janssen, A. Tzalenchuk, and V. Fal'ko, Influence of Impurity Spin Dynamics on Quantum Transport in Epitaxial Graphene, Phys. Rev. Lett. **115**, 106602 (2015).

[37] G. M. Minkov, O. E. Rut, A. V. Germanenko, A. A. Sherstobitov, B. N. Zvonkov, V. I. Shashkin, O. I. Khrykin, and D. O. Filatov, Transverse negative magnetoresistance of two-dimensional structures in the presence of a strong in-plane magnetic field: Weak localization as a probe of interface roughness, Phys. Rev. B **70**, 035304 (2004).